Aeroacoustics Conferences
June 4-7, 2024, Rome, Italy
30th AIAA/CEAS Aeroacoustics Conference (2024)

10.2514/6.2024-3164

Investigation of spectral broadening of sound waves by a turbulent shear layer using particle image velocimetry

Francesco Scarano *, Edouard Salze†, Antonio Pereira‡, Emmanuel Jondeau§ and Vincent Clair.¶
Univ Lyon, École Centrale de Lyon, INSA Lyon, Université Claude Bernard Lyon I, CNRS, Laboratoire de Mécanique des Fluides et d'Acoustique, UMR 5509, 36 Avenue Guy de Collongue, F-69134, Ecully, France

Joannès Chambon ‖
MicrodB, F-69134, Écully, France

The scattering of acoustic waves by a turbulence shear layer is investigated experimentally. The acoustic field is measured with an antenna of microphones, while the shear layer is characterised with Particle Image Velocimetry (PIV). In agreement with previous studies, microphones measurements highlight a broadening of the power spectral density and the formation of two sidelobes around the source tone. The bicoherence spectrum is computed on the microphones signals and evidences a non-linear interaction between the source tone and low frequencies in the shear layer. Spectral proper orthogonal decomposition (SPOD) is applied to the PIV data. The spatio-temporal mode decomposition reveals that the the dominant mode of the spanwise velocity component has a hump that corresponds to the range of frequencies of the sidelobes. This suggests that the spanwise velocity fluctuations are responsible for the interaction with the acoustic field and are the cause of the modification in the acoustic transmission observed in the acoustic measurements. The characteristic turbulent lengthscale that interacts with the acoustic transmission is calculated with several methods and compared with previous studies and turbulent features of the shear layer.

I. Introduction

When an acoustic wave impinges a shear layer, the waves are convected by the uniform flow, refracted by the mean velocity gradient and scattered by the turbulent field of the shear layer. Source tones measured far-field do not emerge as narrow peaks in the energy spectrum. The spectrum exhibits a broadening, the tone power is redistributed into a broadband field centred around the carrier tone, with the presence of two side-bands colloquially called "haystacks" [1].

The haystacking interests several industrial contexts. In a turbofan engine, the propagation of the tone radiated from the exhausted nozzle through a turbulent shear layer is scattered generating a spectral broadening visible in the far-field [2]. The far-field acoustic measurements conducted in an open jet wind tunnel are affected by haystacking: the test model is usually located in the core of the jet; the acoustic field that propagates from the model impinges the shear layer that develops on the sides of the jet and it is scattered causing a broadening of the spectral content and an attenuation of the tone energy [3, 4]. Finally acoustic scattering phenomena can characterise atmospheric acoustic propagation through the atmospheric boundary layer.

Theoretical studies on the scattering of acoustic field by turbulence were firstly carried out by [5] and then by [6] who focused in particular on the modification of the spectrum by isotropic turbulence. Analytical models to predict the haystacking have been proposed by [7] and [8] and more recently by [1] while [9] focused on the scattering produced by a single eddy or a turbulent layer with constant width.

[10, 11] pioneered the experimenal work on haystacking, they suggested that the spectral broadening is dominated by Doppler like effects while the Bragg condition allows to determine the relative positions of the incident and scattered directions. According to [9] the haystacking comes from a combination of two Doppler shifts: the acoustic wave emitted by the source is "absorbed" and then emitted again by the turbulent structures. One Doppler shift is linked with

*postdoctoral researcher, francesco.scarano@ec-lyon.fr
†Research Engineer.
‡Research Engineer.
§Research Engineer.
¶Assistant Professor.
‖Research Engineer.

the motion of the turbulent structure relative to the source and the other is linked with the relative motion between the turbulent structure and the observer; a further contribution to the haystacking comes from the transmission angle between the incident and the emitted ray by the shear layer and the far-field observation angle. To corroborate this hypothesis, experimental results evidenced that the observer position influences the symmetry of the spectral broadening. For the observer located upstream of the source, the spectrum appears more extended in the lower frequencies while if the observer is located downstream the spectrum is more extended in the higher frequencies range. An alternative explaination for the haystacking was proposed by [3] who linked the formation of sidelobes with the time delay variation due to the turbulent shear layer. In particular, it is suggested that the time delay, and by consequence the formation of sidelobes, is function of the convective velocity, the thickness of the shear layer, the source frequency and the spanwise velocity fluctuations. The spanwise velocity fluctuations are, in fact, parallel to the acoustic ray unlike the streamwise fluctuations that are perpendicular to the acoustic ray.

The broadening of the spectrum and the frequency of the two sidelobes can be expressed as

$$|\Delta f| \cong \frac{U_c}{\ell} \tag{1}$$

obtained analytically by [11] and further confirmed experimentally by the same author and other research groups. The relation links the frequency shift of the side-bands with respect to the carrier frequency f_0 with the convective velocity U_c and a characteristic scale of the large eddies, ℓ, sometimes called scattering lengthscale that is found to scale with the vorticity thickness δ_ω (the coefficient of proportionality varies between 3.2 [11] to 4.4 [1, 3, 4]). The relation shows that the scattering is indeed mainly due to the large scale structures present in the turbulent shear layer while the Doppler effect is linked with the convection velocity of the large scale eddies. The frequency shift of the side-lobes, in fact, increases when the convection velocity increases [11] and can be linked with a charateristic frequency of the shear layer [11, 12].

[12], using bi-spectral analysis performed on LES data, showed that the broadening of the spectrum and the depletion of the energy propagated at the carrier frequency into the two side-lobes is a consequence of a non-linear interaction between the incident acoustic wave and low frequencies content in the shear layer. The latter are likely to be linked with the turbulent shear layer and the passage frequencies of large structures in the boundary layer.

The carrier frequency indirectly influences the haystacking because the spectral broadening with visible side-bands occurs when the acoustic wavelength of the source λ_0 is the same order of magnitude of the vorticity thickness of the turbulent shear layer [5]. In this condition, called *weak scattering*, only a small fraction of the acoustic energy is scattered and the interaction of the scattered field with turbulence can be neglected [1]. The fraction of energy scattered increases when the carrier frequency increases, namely when the wavelength decreases. On the contrary, for large turbulent characteristic length to source wavelength ratio, or for high convective velocity, the energy associated with the side-bands increases up to a point where the lobes are not anymore discernible in the spectrum. This condition, called *strong scattering*, in extreme cases, is characterised by the disappearance of the tone that is substituted by a unique broad hump [9].

According to [10], for intermediate frequencies and flow velocities, half of the measured power is propagated in the form of scattered waves due to the scattering by turbulent eddies. [3] derived a theoretical relation that links the decrease of the transmitted energy at the carrier frequency, which is attenuated due to the scattering, with the time delay

$$E_p/E_{\text{tot}} = e^{-\beta^2}. \tag{2}$$

where E_p is the scattered energy associated with the source frequency and E_{tot} is the total energy transmitted without scattering. The parameter β is directly linked with the time delay through the turbulence intensity

$$\beta = \frac{\pi^2}{\sqrt{2}} T_v M_0 \frac{\delta_\omega}{\lambda_0} \tag{3}$$

where T_v is the spanwise turbulence intensity and M_0 is the Mach number of the flow. This relation seems to be in quite good agreement with several experimental tests conducted in different facilities [3]. According to [5], for frozen turbulence, the scattering process due to the turbulence is only responsible for redistributing spatially the acoustic energy without acting as a source or sink. This means that the acoustic energy is conserved. On contrary, according to [8, 13] part of the energy is scattered and part is absorbed by the turbulence.

Different hypothesis have been made to link the haystacking with particular turbulence features in the shear layer. In addition dubts arise if the predominant effect is a Doppler-like effect, due to the streamwise fluctuations or the spanwise component fluctuation associated with the time delay of the acoustic signal. In the current paper, through Particle Image Velocimetry and acoustic measurements, we further explore the link between the shear layer charateristic features and the formation of sidelobes in the acoustic spectrum.

II. Experimental setup

The experiments are conducted in the anechoic open jet wind tunnel of the Laboratoire de Mécanique des Fluides et d'Acoustique (LMFA) at the École Centrale de Lyon. A centrifugal fan powered by a 800 kW generates a flow having a maximum mass flow rate of about 20 Kg/s. The flow is subjected to a series of acoustic treatments. The jet is equipped with a nozzle having a contraction ratio of 1.25 ending with a square exit section that measures 0.5 m side. The anechoic room where the jet enters measures 730 m^3. The maximum speed achievable with the current contraction ratio is around 80 m/s. This choice, that imposes a limit to the maximum speed, is dictated by the need of having a sufficiently extended potential core region where to place the acoustic source. Three flow conditions are tested: 35, 55 and 75 m/s. The corresponding Mach numbers are 0.10, 0.16 and 0.22. The corresponding Reynolds numbers based on the vorticity thickness (see (5)) at x =500 mm vary between 174000 and 373000. The temperature of the jet is monitored through all the experimental campaign though a thermocouple located at the exit of the nozzle.

	x_s [mm]	U_0 [m/s]	f_0 ´[kHz]	ΔY_{sa} [mm]
antenna	500	35, 55, 75	8, 12, 16	1500,570
	1000	35,55,75	8, 12, 16	1870
PIV	500	35, 55	-	-
hwc	500	75	-	-

Table 1 Measurements and test parameters.

A. Acoustic source

The acoustic source consists in a speaker embedded on one side of a NACA-shaped support. The support is stiff enough to prevent vibrations and its shape reduces the aerodynamic influence on the jet. The source speaker is located along the centreline of the jet. The acoustic field is generated by a compression chamber connected with the speaker and located beneath the support and amplified analogically. The source is connected to three microphones inside the NACA-casing that are used as reference. The amplitude of the acoustic source is chosen in order to be clearly distinguished from the broadband noise generated by the jet and the trailing edge of the source support. Two source streamwise positions are tested: x_s =500 mm and x_s =1000 mm.

Three frequencies are tested 8, 12,16 kHz. The choice of the acoustic properties of the source is dictated by the need of performing tests at audible frequencies (2-20 kHz) that are at the same time exploitable for acoustic imaging techniques. The source frequency f_0 is linked with the source wavelength by the relation $\lambda_0 = c/f_0$, where c is the seed of sound. The choice of a frequency for a given shear layer dictates the ratio δ_ω/λ_0. According to previous investigations, in order to have a weak scattering and the sidelobes well identifiable, this value has to be of the order of unity. For thickness to wavelength ratio much larger than unity, the occurrence of strong scattering is usually documented. For values of δ_ω/λ_0 much smaller than unity, according to [14], multiple lobes occur but with a relative energy that can be smaller than the background noise and for this reason not easily identifiable experimentally.

B. Microphone antenna

A SoundCam antenna is used to perform the acoustic measurements. The antenna consists of five branches connected to a central portion (see figure 1 (c) and (d)). 84 MEMS microphones are located along the branches and the centre of the antenna. A branch of the antenna is aligned with the flow along the streamwise direction; the branch is located at the same height, z, of the source (lays in the same xy plane of the source). Care is given in aligning one microphone of the branch with the source streamwise position in order to have $x_m = x_s$ (M77 in figure 1). The measurements with the antenna are performed at the two source positions, x_s = 500 and x_s =1000 mm downstream of the exit section. The antenna is located at two distances with respect to the source, Y_r = 1500 mm (nominal condition) and Y_r = 579 mm (closer condition). The distances reported are related to the microphone aligned with the source.

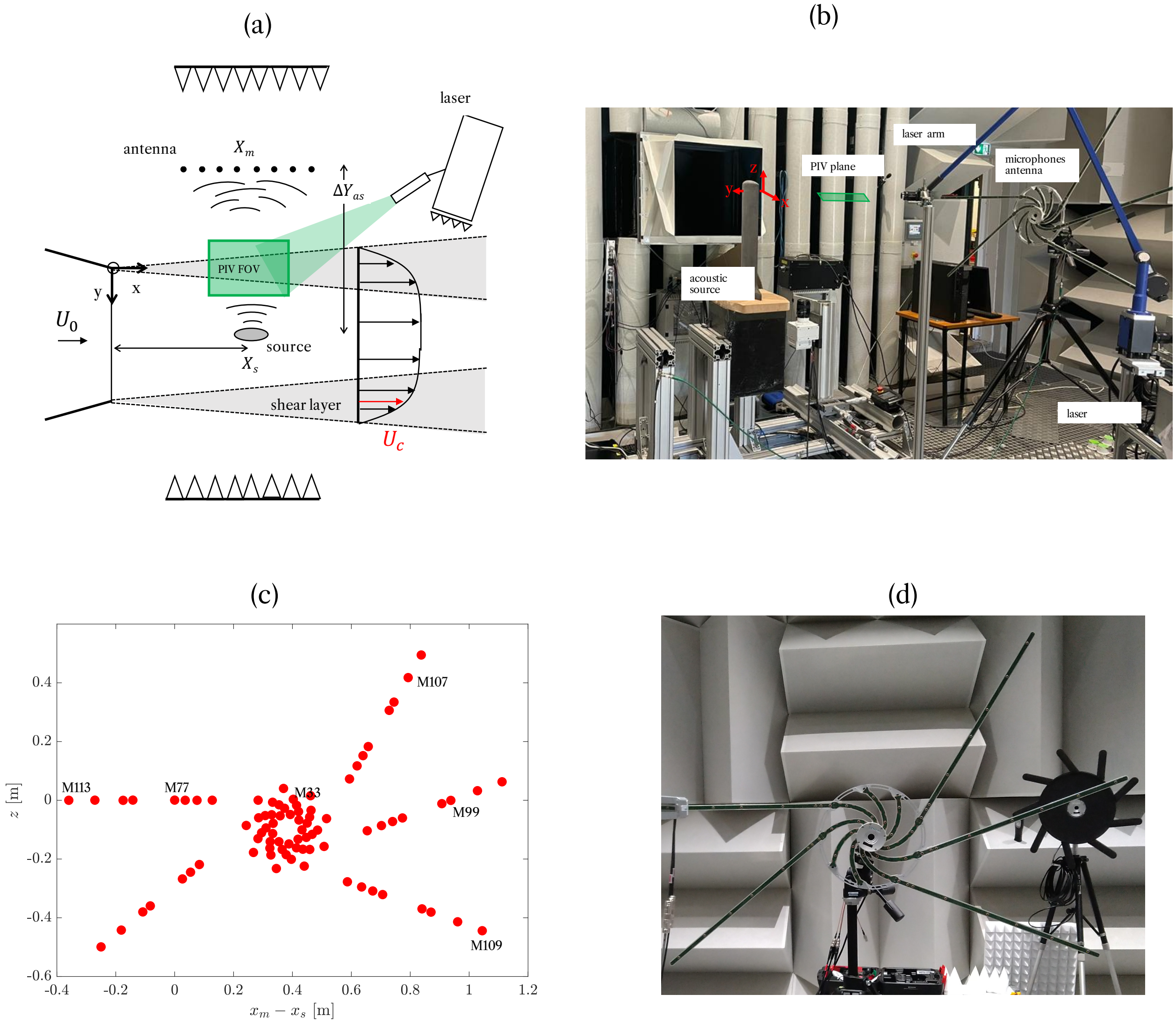

Fig. 1 (a) Schematic of the PIV and antenna experimental setup, (dimensions not in scale), (b) photos of the experimental setup, (c) schematic of the antenna used for the tests, (d) photo of the antenna.

C. Directivity antenna

To study the effect of the shear layer on the directivity, a microphone arc is located around the source externally with respect to the shear layer development. The arc is composed of 14 microphone equally spaced each other by an angle of $\Delta\theta$ =10°C. The distance of each microphone with respect the source is Y_r = 2050 mm. The directivity is performed at xs = 500 and 1000 mm to evaluate the effect of the shear layer growth. The microphone arrangement, and the active microphones are reported in figure 2. The microphone at θ =0°C is aligned with the source location x_s.

D. Particle Image Velocimetry

Planar Particle image velocimetry (PIV) is employed to characterise the shear layer properties. The measurement plane is horizontal (xy) in the plane containing the source. The PIV plane is centred with the streamwise location of the source (measurements only for the source position at x_s =500 mm) while in the spanwise coordinate is shifted by −30 mm. This is done in order to better capture the shear layer that diverges towards negative values of y. The shear

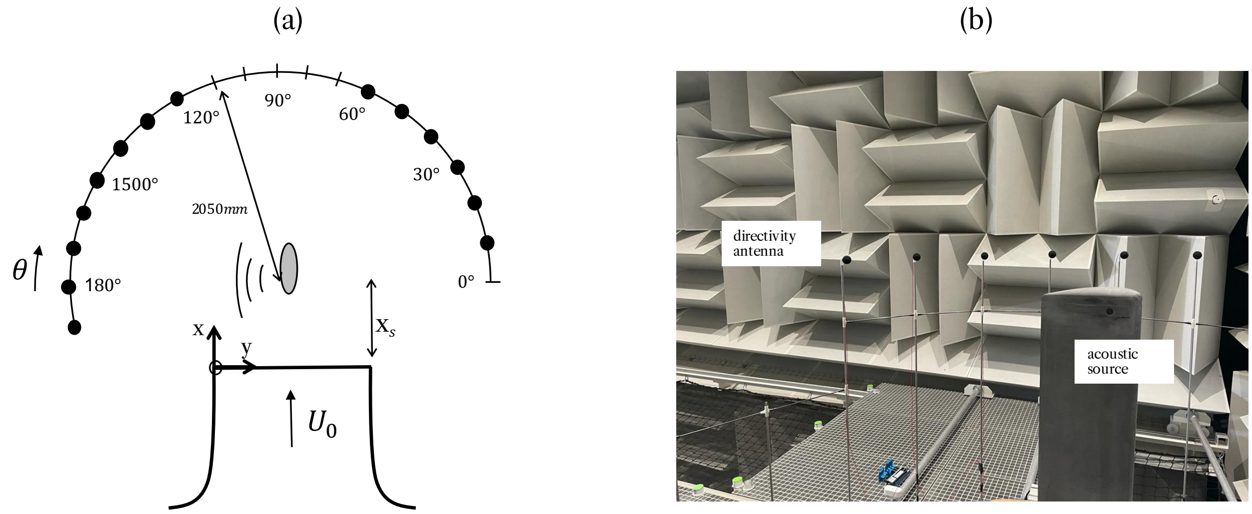

Fig. 2 (a) Schematic of the directivity experimental setup, (dimensions not in scale), (b) photos of the experimental setup.

layer is charaterised with PIV only at 35 and 55 m/s, while for 75 m/s hot wire measurements are performed to obtain the vorticity thickness.

Two smoke generators are employed, one to seed the core of the jet and the second to seed the anechoic chamber in order to have sufficient particle density in the shear layer. To keep the particle image size between 2 and 4 pixels and reduce peak-locking effects the particle images are slightly defocused [15]. A double pulsed Continuum Mesa PIV laser is employed to illuminate the particles. The acquisition frequency is set to 5 kHz. A Phantom VEO1310L 12 bits CMOS camera equipped with a 60 mm f/2.8 Micro Nikkor lens is used as imaging tool. Lavision DAVIS 10.2 is used for the calibration, synchronisation, laser control and image acquisition. Each run consists in 4900 image pairs for a duration of 0.98 s. Almost 20 runs are acquired for each flow condition in order to have a sufficient convergence of the statistics allowing to resolve the largest flow features. The samples are processed using the 2D2C cross-correlation PIV algorithm of DAVIS 10.2. The interrogation window size is iteratively changed passing from 64×64 pixel to 8×8 with an overlap of 50%; this leads to a vector spacing of $\Delta x = \Delta y$ =0.665 mm and a grid of 34200 vectors with a field of view (FOV) of 158 mm $\times$ 212 mm ($2.2\delta_\omega \times 1.6\delta_\omega$).

E. Hot wire anemometry

The shear layer characterisation at 75 m/s is conducted with hot wire anemometry due to the seeding system limitations in the current setup (limitations on the mass flow rate). A Dantec gold-plated hot wire 55P11 straight probe is used to survey the shear layer. The wires are conditioned using a Dantec Streamline after the resistances are measured. An overheat ratio of 0.8 is imposed. The wire temperature after the conditioning is approximately equal to $T_w = 238°C$. The frequency response of the system, obtained from a square wave test, is equal to 85 kHz and it is evaluated at the maximum test velocity. The shear layer is surveyed at three streamwise locations: 300, 500 and 700 mm. The hot wire is traversed through the shear layer Y direction. The minimum displacement is 0.01 mm. The sampling frequency is 104 kHz, the sampling time for each y-position is equal to 20 s.

The voltage acquired for each measurement is corrected to take into account temperature variations (as the overheat ratio is not adjusted prior to each data acquisition). At this purpose a thermocouple is installed on the cross-wire support to measure the local temperature along the shear layer. This allowed to characterise the temperature gradient though the shear layer (colder ambient condition, hot jet flow in the core). The velocity calibration is performed *in situ* in the core of the jet against a pitot tube. The calibration law is obtained using a forth order polynomial fit [16].

III. Results

A. Shear layer characterisation

A free shear layer develops when two uniform velocities U_a and U_b where in general $U_a > U_b$, initially separated, interact forming a mixing region. In the current setup the two velocities are equal to U_0 and 0. It is possible to define the convective velocity U_c as

$$U_c = (U_a + U_b)/2 = U_0/2 \tag{4}$$

and the velocity ratio $R = (U_a - U_b)/(2U_c)$ that in the current case is equal to one. The vorticity thickness is defined as

$$\delta_\omega(x) = \frac{U_0}{\left(\frac{\partial U(x)}{\partial y}\right)_{\max}}. \tag{5}$$

Turbulent shear layers evolves self-similarly downstream a certain streamwise coordinate x_0. According to [17], in order to achieve a self-similar shear layer, three conditions are necessary. The first condition is the linear growth of the shear layer vorticity thickness, the second is the collapse of mean profiles when plotted using reduced coordinates $y\sigma/x$, where x and y are the streamwise and spanwise coordinates and σ is the spreading parameter ([18]) and the third is the plateau in the peaks of the statistics.

The characterisation of the shear layer at the two flow conditions is reported in figure 3. The spreading parameter that fits the best the experimental data is $\sigma = 11$ which is in perfect acreemend with previous studies [3, 4, 12, 18] while the origin of the self similar region is found to be $x_0 = 0.01$ m. The linear growth of the vorticity thickness is reported in figure 3 (a); in figure 3 (b) the collapse of the non-dimensional mean velocity profiles at various streamwise location is reported for the 55 m/s condition, while the effect of the freestream velocity is reported on the non-dimensional standard deviation profiles σ_U/U_0 and σ_V/U_0 which are found to collapse. The streamwise evolution of the peaks of the standard deviations as well as the Reynolds shear stress $-\overline{uv}$, where u and v are the fluctuations of the streamwise and spanwise velocity components, is reported in figure 3 (d). The peak values are again in good agreement with previous studies. The drift coordinate y_0, defined as the location where $U = U_c$ is depicted in figure 3 (e) alongside the contour of the mean streamwise velocity for 55 m/s. The streamwise velocity spectrum, obtained with the hot wire probe at 75 m/s in correspondance of the peak of σ_U/U_0 is reported in figure 3(f) for three streamwise locations. The inertia range (marked with the -5/3 dotted slope) as well as the dissipation range can be identified, confirming a canonical turbulent state of the shear layer.

B. Power spectral density of the acoustic signal

In figure 4 the power spectral density (PSD) for acoustic signals from the antenna are reported. The spectra are computed using the Welch algorithm with 94 segments, a window size of 2^{15} samples and 50% overlap. The spectra are then centred with the source frequency and normalised by the peak energy. The formation of secondary lobes due to the passage of the acoustic wave through the shear layer can be evinced in all the subfigures. Excluding the figure 4 (d), all the signals are obtained from the microphone at $x_m = x_s$ (M77).

The effect of the of the carrier frequency at iso-freestream velocity is reported in figure 4 (a). Increasing the source frequency, namely decreasing the wavelength, increases the scattering of the energy. This is due to the fact that the acoustic wavelength is smaller compared to the characteristic scale of the turbulence and an higher amount of energy is scattered. The Δf remains rather constant for the different carrier frequency tested, in agreement with equation 1. As reported by several authors, the frequency bands increase when increasing the freestream/convective velocity at iso-frequency as depicted in figure 4 (b) and following the equation 1. The frequency shifts for the three flow conditions are found to be approximately equal to 50, 80 and 100 Hz which is in good agreement with the equation 1. Changing the source position from $x_s = 500$ mm to $x_s = 1000$ mm, at iso-source frequency and iso-freestream velocity, increases the amount of energy scattered by turbulence as the acoustic waves passes through a thicker shear layer as reported in figure 4 (c). A similar mechanism can be highlighted when the microphone position is changed, as reported in figure 4 (d) due to the oblique transmission of the acoustic wave from the source to the microphones. For the microphones located further downstream (M109, M99) the sidelobes almost disappear with the formation of a single hump; this condition is similar to the strong scattering reported numerically by [9]. However, in contradiction with the studies by [11], [3] and [9], the microphone location, upstream or downstream with respect to the source, does not influence the symmetrical distribution of the sidelobes.

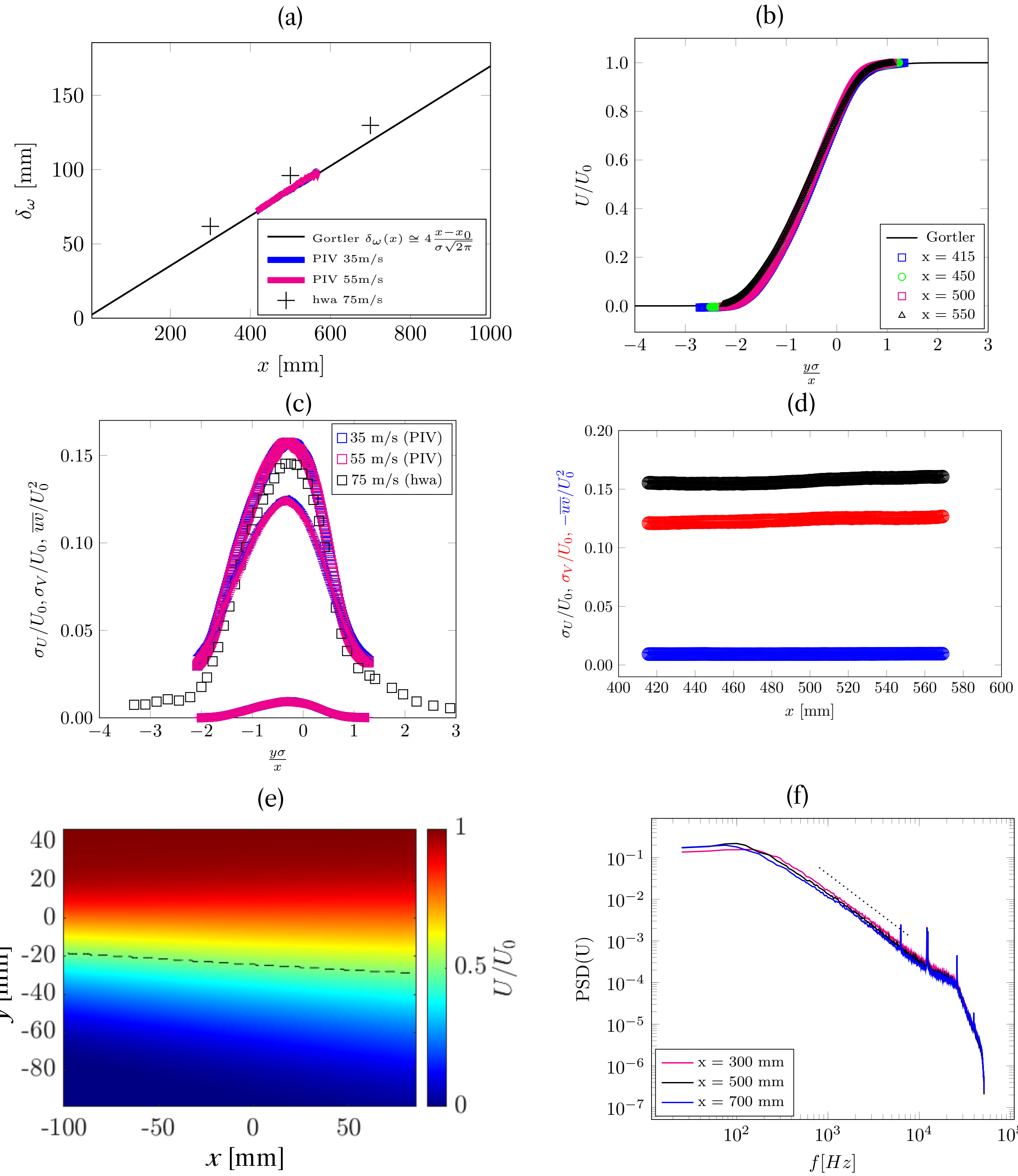

Fig. 3 Linear growth of the vorticity thickness (a), collapse of the shear layer mean velocity profiles at different streamwise locations for 55 m/s (b), collapse of standard deviation of the U and V component at the two freestream velocity (c), plateau of the shear stresses peaks along the streamwise direction (d), drift coordinate and contour of the non dimensional mean streamwise velocity (e), streamwise velocity spectrum at 75 m/s obtained in correspondance of the σ_U/U_0 peak.

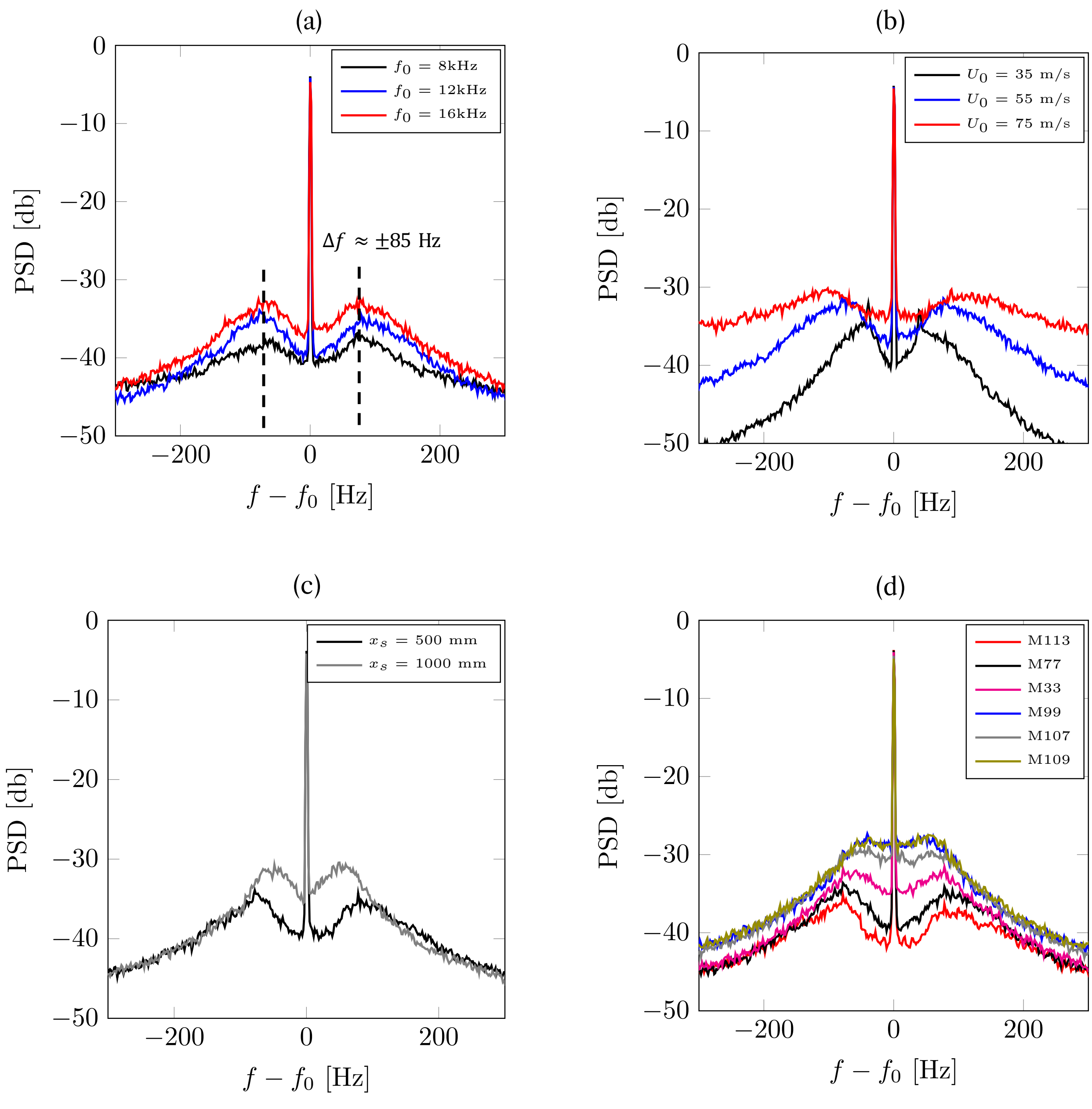

Fig. 4 PSD for three different source frequencies for the microphone at $x_m = x_s$ (a) effect of source frequency at a U_0 =55 m/s and, (b) effect of the free-stream velocity U_0 at f_0 =16 kHz, (c) effect of the measurement location x_s at U_0 =55 m/s and f_0 =12 kHz, (d) effect of the microphone position, f_0 =12 kHz U_0 =55 m/s.

The energy peak ratio with respect to the total energy (peak plus the energy of the sidelobes) is reported in figure 5. The total energy, E_{tot}, is defined as the integral of the PSD including the sidelobes in an interval $\pm f$ that is defined as the frequencies at which the PSD approaches the PSD without the source

$$E_{\text{tot}} = \int_{f_1}^{f_2} PSD(x_s, f)df \tag{6}$$

while the peak energy, E_p, is obtained by integrating the PSD at $f_0 \pm 5$Hz as computed by [19]. The values obtained without subtracting the noise of the shear layer (figure 5 (a)) match decently the theoretical relation by [3]; however a certain scatter of the data around the theoretical values can be noticed. The data are less scattered if the background aerodynamic noise is removed, as can be seen from figure 5 (b), but the theoretical courve overestimate the carrier energy peak decrease due to the turbulence scattering.

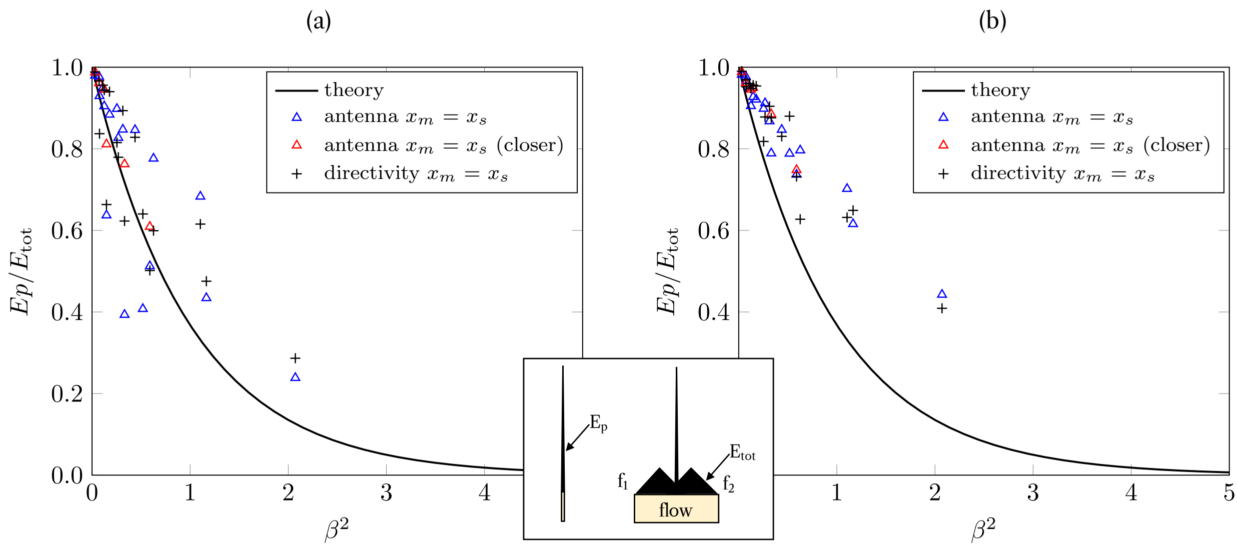

Fig. 5 Rato between the peak energy and the total energy, (a) no shear layer noise is removed, (b) shear layer noise removed.

C. Directivity modification

In figure 6 the directivity results are reported. For the no flow condition (figure 6 (a)) the directivity pattern is almost unidirectional on the side where the source is emitted (90-180°) while the values are lower and noisier on the opposite side with respect to the sound emission (0-90°). When increasing the free-stream velocity U_0, the carrier frequency, f_0 or the source streamwise position x_s the unidirectionality is lost with the formation of a bi-lobe pattern for the highest free-stream velocity and the highest frequency respectively (figure 6 (a) and (b)). As expected and detailed above, the decay of SPL is more pronounced in correspondence of 120° where the shear layer is thicker and the sound traverses the shear layer with an oblique trajectory further increasing the scattering. This effect is even more pronounced when the source location is further shifted downstream (figure 6 (c))

D. Bicoherence

According to [4] and [12] the formation of the sidelobes is due to a non-linear interaction between the acoustic source and a characteristic low frequency of the turbulent shear layer. To highlight this coupling, the authors carried out an analysis computing the bicoherence spectrum on experimental and numerical data respectively. Following [20] the bicoherence can be computed as

$$\text{Bic}^2(x_i, f_1, f_2) = \frac{|\langle \hat{F}(x_i, f_1)\hat{G}(x_i, f_2)\hat{H}^*(x_i, f_1 + f_2)\rangle_b|^2}{\langle |\hat{F}(x_i, f_1)\hat{G}(x_i, f_2)|^2 |\hat{H}(x_i, f_1 \pm f_2)|^2\rangle_b} \tag{7}$$

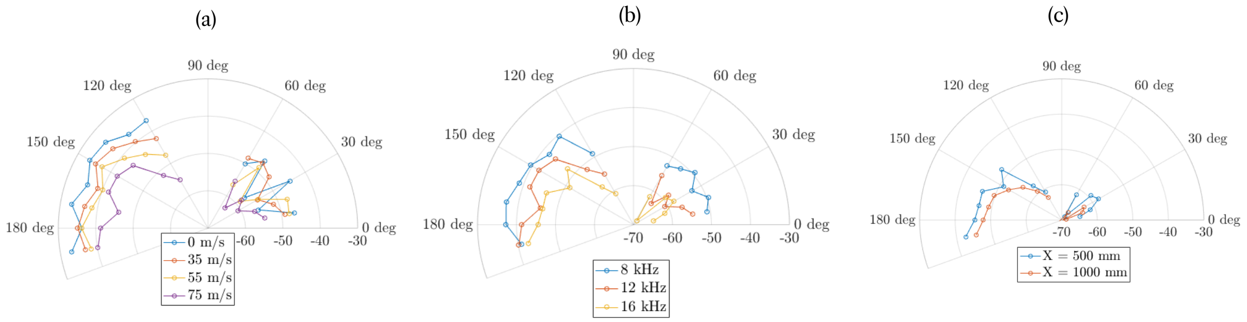

Fig. 6 Directivity results (a) fixed carrier frequency $f_0 = 12$ kHz and $x_s = 0.5$m effect of the flow velocity, (b) fixed free-stream velocity $U_0 = 75$m/s and $x_s = 0.5$m, effect of the frequency, (c) fixed $U_0 = 75$m/s and $f_0 = 16$kHz, effect of the source position.

where F, G and H are three signal f_1 and f_2 are two frequencies and $\langle\rangle_b$ represents the average of the blocs in which the signals is divided. The level of bicoherence are significant only if

$$\mathrm{Bic}^2 > \frac{9.2}{18/11 n_b} \tag{8}$$

where n_b is the number of blocks.

High value of bicoherence represents a non-linear interaction between the frequencies f_1 and f_2 and a non-linear transfer of energy to the frequency $f_1 \pm f_2$. The bicoherence spectrum is computed on the signal that corresponds to the $x_m = x_s$ $(F = G = H)$. The values of bicoherence spectrum are non negligible only for the measurements obtained with the antenna closer to the shear layer. For this configuration, indeed, the aerodynamic low frequency fluctuations (pressure fluctuations) of the shear layer are captured by the antenna. This can be seen in the figure 7 (b) where the full spectra for the two antenna positions are compared. In the low frequency regime a bump is more evident if the antenna is closer to the shear layer. In addition, the acoustic energy captured by the microphone is higher as the entire spectrum is shifted upward, including the sidelobes (figure 7 (a)).

The bicoherence spectrograms are depicted in figure 8 for the source frequency of 12 kHz at 35 and 75 m/s. High level of bicoherence are associated with the intersection of the frequencies f_1 =12 kHz and f_2 = 50 and 100 Hz depending on the flow condition. It has to be underlined that these values are identical to the sidelobes reported from the broadening of the PSD at 35 m/s and 75 m/s. The spectrograms are in perfect agreement with the numerical results of [12] and they suggest a strong non-linear interaction between the aerodynamic low frequency and the carrier frequency. In addition, the oblique region of high bicoherence underlines that there is in turn a non-linear interaction between the low frequency and the sidelobes at $f_1 - f_2$. The bicoherence is found to be stronger for the microphones slightly downstream of the $x_m = x_s$ (not shown here), this is might be due to the convection of the acoustic waves. Conversely, the bicoherence becomes negligible for the microphones far from $x_m = x_s$ (like M116, M117, M109).

E. Spectral proper orthogonal decomposition

We confirmed that the haystacking is due to a non-linear interaction between a low frequency dynamics of the turbulent shear layer and the high frequency acoustic wave of the source. To further investigate the nature of the physical mechanism that dominates the shear layer dynamics, the spectral proper orthogonal decomposition (SPOD) analysis is performed on the PIV data-set. SPOD allows to extract from statistically stationary data, as the PIV data-set of the current investigation, an optimal orthogonal basis where a high fraction of the total energy is retained in a few modes that express coherence both in time and space [21].

The SPOD is performed on both the streamwise, U, and spanwise, V, component of the flow. For the SPOD analysis, the Matlab routines reported by [22] are used. Being the Nyquist frequency of 2.5 kHz the data sample are well resolved in time for extracting the low frequency dynamics of interest. Each data-set (RUN) is divided in 37 Hamming windows of 256 snapshots with 50% overlap; changing the window size does not influence the results. The SPOD spectra are reported in figure 9 (a) for the U component and figure 9 (c) for the V component and for the two test velocities, 35 and 55 m/s. The prevalence of the first mode is illustrated by representing in grey the ten most energetic modes (only for the

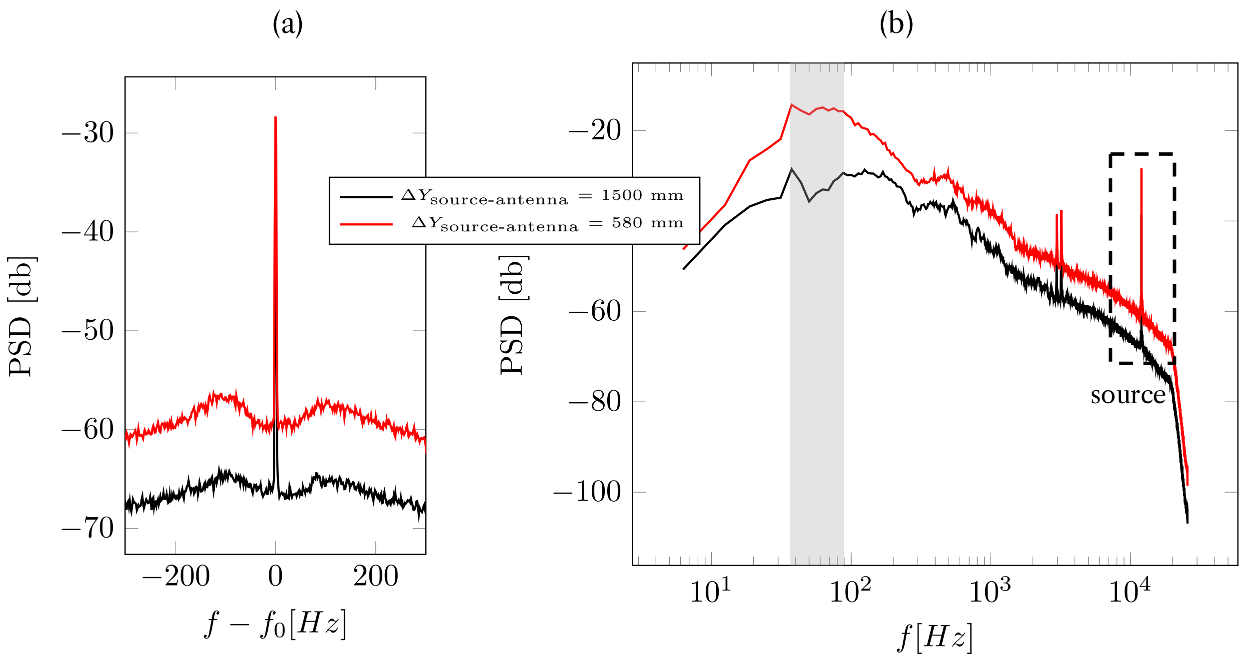

Fig. 7 PSD of the signal at $x_m = x_s$**,** f_0 =12 kHz **at** 75 m/s**, effect of source-antenna distance (a) PSD centred around the carrier frequency, (b) full spectrum.**

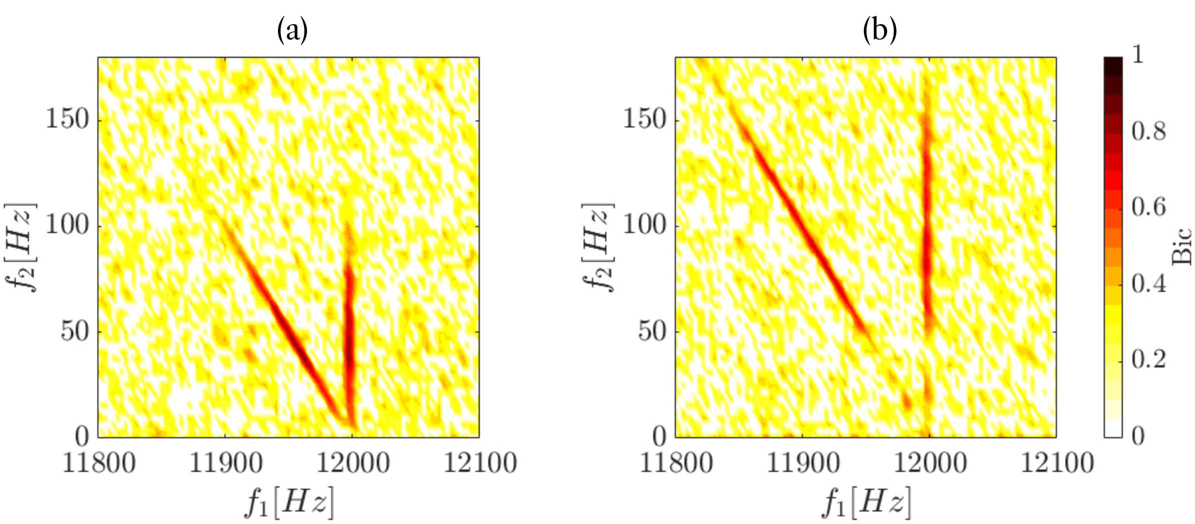

Fig. 8 Bicoherence spectrogram of the signal at $x_m = x_s$**,** f_0 =12 kHz**, (a)** 35 m/s**, (b)** 75 m/s**.**

55 m/s case, similar results are found for the 35 m/s). The first mode (thicker line) for both the velocity components contains about the 30% of the total turbulent kinetic energy. The results reported herein are found to not vary from one RUN to another, the spectra reported for the first mode are the average of the spectra obtained for all the RUNs.

The spectra of the U component evidences a broad region of high energy extending from 10 Hz up to low frequencies (around 35 Hz), the spectrum slightly shifts to a larger values of frequencies but the peak remains always in correspondence of a frequency below 40 Hz. The mode, associated with this frequency, is reported in figure 9 (c) for 55 m/s. It shows elongated structures that are not entirely captured by the limited PIV field of view. Conversely, the spanwise component most energetic mode is dominated by a hump which is centred around a low frequency that is approximately equal to 55 Hz for U_0 =35 m/s and for about 85 Hz for U_0 =55 m/s. The mode that corresponds to the peak frequency is represented in figure 9 for 55 m/s. It has to be underlined that the peak of the humps corresponds exactly to frequency shifts Δf due to the haystacking and documented in the PSD of the acoustic signal. The results indicate that the first mode of the V component interacts with the acoustic transmission and is responsible for the formation of side-lobes in the acoustic spectra. This is relevant as it suggests, in agreement with the model by [3], that the spanwise fluctuations v dominate scattering of the wource tone.

F. Evaluation of the length-scale that interacts with acoustic transmission

1. Scattering length from PSD

The equation 1 allows to obtain a characteristic lengthscale linked with the sidelobes, the scattering lengthscale. The value relies on the evaluation of Δf of the sidelobes in the PSD and knowing the convection velocity U_c of the shear layer. Some of the values reported in the literature are summarised in table 2 made non dimensional using the vorticity thickness. As reported in the tab, excluding [23] a value of ℓ/δ_ω approximately equal to 4 is found by most of the author. The evaluation of the lengthscale using the acoustic spectrum cannot be considered very precise, as there is an intrinsic uncertainty in the evaluation of the abscissa of the peak (that depends on the windowing, or on an eventual smoothing of the spectra), the computation of the convection velocity and the vorticity thickness (which involves numerical spatial derivatives on experimental data). In the current results, the values of ℓ/δ_ω computed from the acoustic spectrum present a certain dispersion as shown in figure 10 when plotted against the scattering parameter $s = \delta_\omega M_0/\lambda_0$. The value for each measurement is obtained by considering the peak of the sidelobes after having smoothed the spectra. Despite the scatter, the average value, for the three free-stream velocities, converges to $\ell/\delta_\omega = 4.1$ with a standard deviation of 0.7, as reported in table 2.

This lengtschale is taught to be the characteristic scale of the turbulence that interacts with the acoustic transmission. However the evaluation does not rely on any associated aerodynamics measurements and the scope of this section is to strengthen the link with the aerodynamic features of the shear layer by analysing the PIV data.

2. Eduction of the lengthscale using SPOD

A characteristic length-scales can be educed from the SPOD modes reported above. The modes, both for the U and the V component show a streamwise periodicity. It is then possible to compute the wavelength of the dominant mode at the frequency of the peak, frequency we saw already that for the V component corresponds with the frequency of the sidelobes. As the limited field of view does not allow to perform a spatial FFT, Taylor's hypothesis of frozen turbulence is assumed and the mode is reconstructed in space using the time-resolved data that are propagated in space using the convection velocity U_c for five periods. The wavelength is educed for a spanwise location that corresponds to the centreline of the FOV (Y = -30 mm), namely the centre of the shear layer; changing this position in the proximity of the centreline as well as changing the window size in the SPOD modes computation does not lead to variations in the wavelength.

The figure 11 reports the result for a particular RUN at 55 m/s for the two velocity components, the contour of the spatially propagated mode is reported in figure 11 (a) and (b), while the FFT are reported in figure 11 (c) and (d) for all the RUNs. The non-dimensional wavelength associated with the V component, $\lambda_{\mathrm{SPOD},V}/\delta_\omega$ is around 4.1 for both 35 and 55 m/s, despite some variability between the different RUNS. However, as reported in table 2, the standard deviation of the $\lambda_{SPOD,V}\delta_\omega$ is not dissimilar with respect to the results obtained by calculating the lengthscale with the PSD. This can be considered a further confirmation of the importance of the spanwise velocity fluctuations in the haystacking. The wavelength associated with the U component is $\lambda_{\mathrm{SPOD},V}/\delta_\omega \cong 6$, way larger than the typical values obtained in the literature for scattering wavelength. Despite the striking match of the POD wavelength with the charateristic wavelength of the haystacking, the physical meaning of the associated mode is not completely clear. For

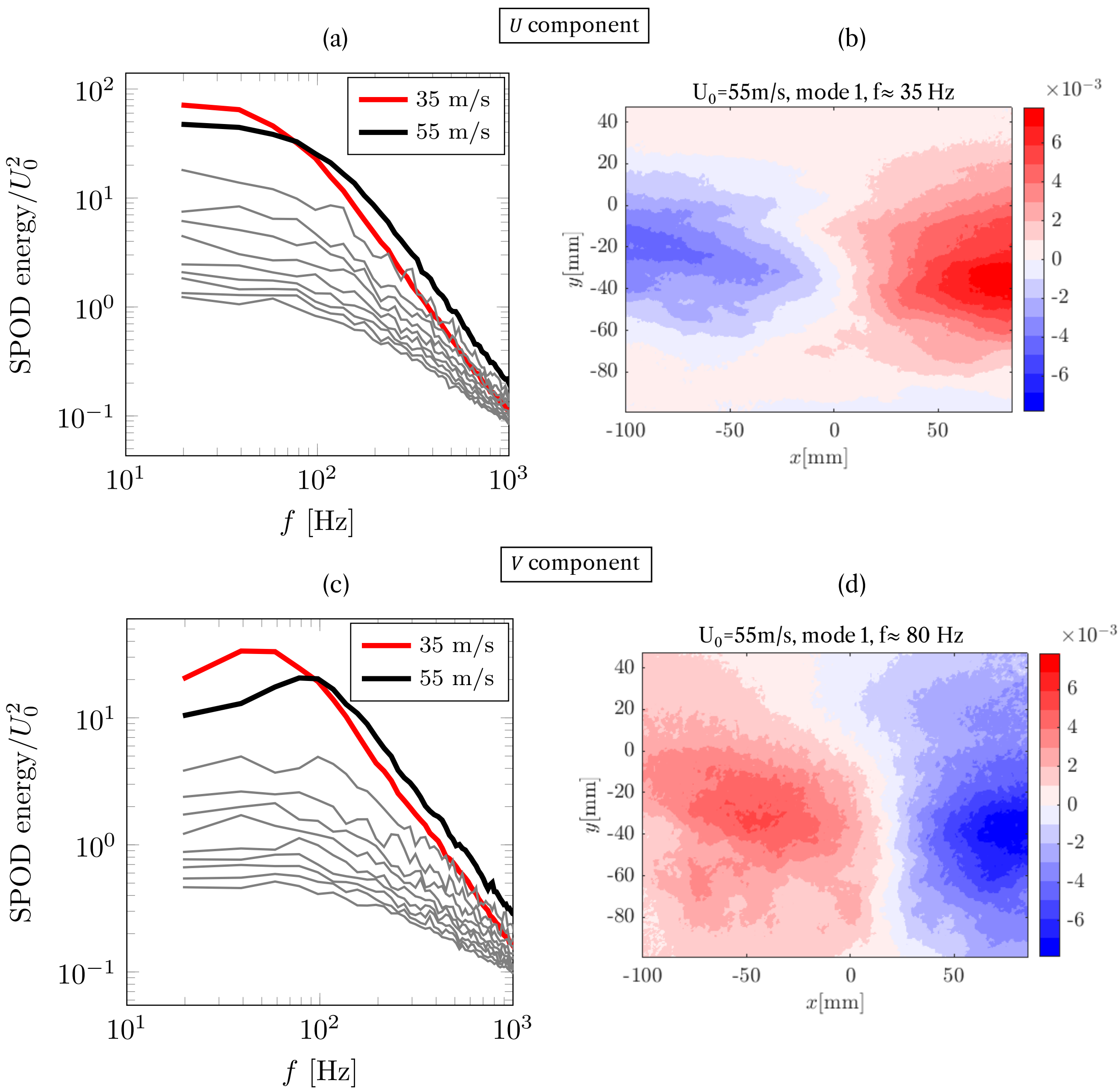

Fig. 9 SPOD spectra for 35 m/s **(a) and** 55 m/s **(c), only the ten most energetic modes are displayed, thick lines represent the leading mode (averaged on all the RUNS); snapshot of the leading sPOD mode** (30% **total energy) at the peak frequency for** 35 m/s **(b) and** 55 m/s **(d).**

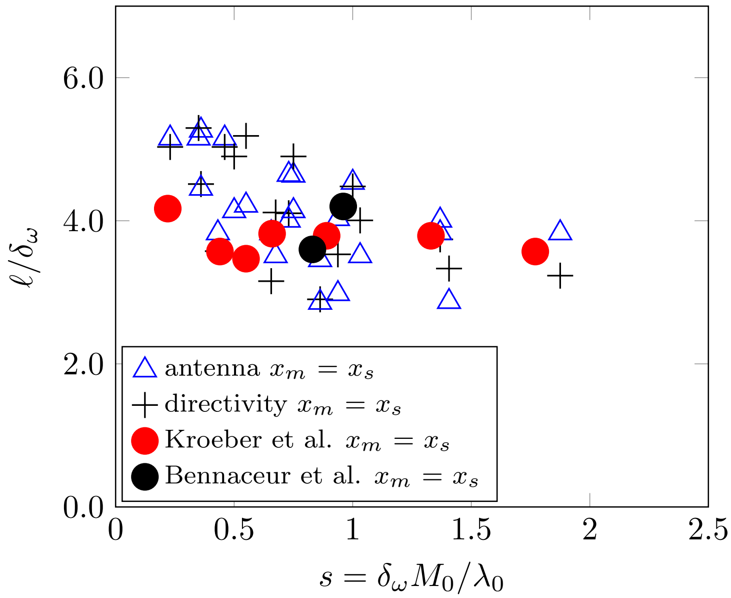

Fig. 10 Values of ℓ/δ_ω obtained from acoustic PSD data by using equation 1 as a function of the scattering parameter s; data by [4] and [12] are included.

this reason, other approaches to obtain some characteristic turbulent scales are proposed.

3. Average distance between structures

According to [24] the characteristic length that interferes with the acoustic wave corresponds to the distance between the large structures in the shear layer. This distance was firstly estimated by [25] from flow visualization; the value is around 3.2 times the vorticity thickness (see table 2). In the work by [23] the scattering lengthscale educed from the side-lobes in the acoustic spectrum is found to match exactly the value by [25], so the authors suggested that the passage of large structures was the cause of the scattering of acoustic waves. However, the recent body of work on haystacking, including the current investigation, reported values of the lengthscale educed from the PSD that is larger than four times the vorticity thickness (4.1 in the current investigation).

[26, 27] computed distance between the large structures by computing the time interval between the passage of two consecutive structures, T_p, and multiplying it by the convection velocity: $\ell_p = T_p U_c$. [27] found an average large structure distance between 3 and 3.2 times the voricity thickness, the values are in good agreement with the value by [25], but, according to the author, too low to consider the passage of large structures as the phenomenon that leads the acoustic scattering. [26] found a relation that links the mean distance with the velocity ratio R

$$\ell_p = 0.54R + 4.0 \tag{9}$$

that for the current case gives a value of 4.45 that is close to the scattering length-scale obtained from the PSD data of the current investigation but dissimilar with respect to the values obtained by [27].

The passage time is calculated starting from the autocorrelation function R_{uu} of a point located at a fixed streamwise position (the centre of the domain) and at a spanwise position located at the edge of the shear layer where the velocity signal is more sensitive to large structures. According to [26] the position at $y = 1.3\delta_\omega$ on the low-speed side is the most appropriate because the signal is contaminated by the small scale vortices of the rotational part of the flow. [26] highlighted that even a small variability in the choice of the spanwise location leads to an erroneous evaluation of the distances between the structures. [27] calculates the large vortices distance at a similar spanwise location but on the high speed side, this could explain the difference in the results. The main difference between the two studies, however, relies in the definition of the passage time T_p from the autocorrelation function. The autocorrelation function has a shape that is quasi-periodic with relative peaks as high as 0.2. According to [27] T_p can be calculated as the average interval between two maxima in the R_{uu} (averaged on the entire signal) whereas in the paper by [26] T_p is the time interval to the to the first peak of the autocorrelation function.

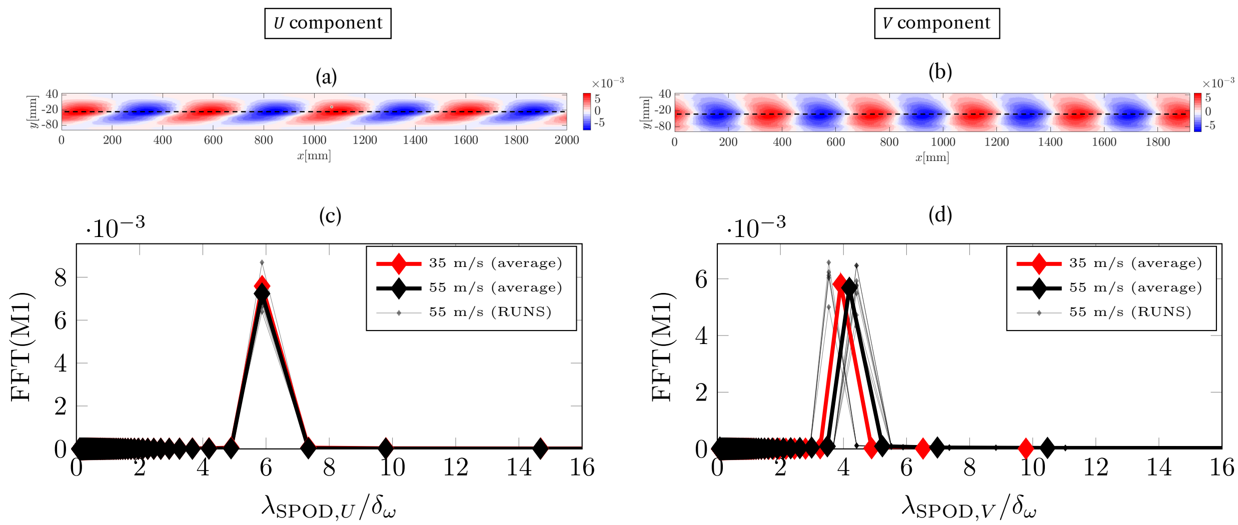

Fig. 11 Spatial propagation of SPOD mode1 at the frequency of the peak at U_0 =55 m/s, U component (a), and V (b); evolution of the mode amplitude along the streamwise direction for $Y = -30$mm (c) and (d), and FFT of the mode amplitude, (e) and (f).

The autocorelation at $x = x_s$ at the edge of the shear layer is reported in figure 12 (a). The autocorrelation is smoothed (red curve on the figure) with a moving average function to better identify the maxima (the blue circles in the figure). In figure 12(b) the two methods to define the passage time T_p are compared for 55 m/s. Additional hot wire measurements are performed at the spanwise position prescribed by [26, 27], which is outside the PIV field of view. The errorbars are computed using the standard deviation of the passage time within one signal and between the RUNs (only for the PIV data). As depicted in figure 12(b) the shape of the distance profile is similar for the two methods. The distance between the structures is underestimated if the average T_p of the signal is considered, this because the autocorrelation function asymptotically tends to zero as the time increases and the uncertainty in the identification of the local maxima increases. What has to be underlined is that the distance ℓ_p increases at around $y/\delta_\omega = 1$ but at the same time the uncertainty increases for both methods making undesirable to use that spanwise position to determine the distance between the structures. Similar considerations were reported by [26]. The results match quite well the ones reported in the literature following the two different methods. In particular, the value obtained using the first peak as passage time [26] is very close to the scattering length. This might suggest that the passage of large structures plays an important role in the haystacking contradicting what reported by [27]. It is finally worth noticing that using the average peaks method on the R_{vv} (using the spanwise velocity component) gives an estimation of the distance that is closer to the scattering length (figure 12 (c)).

4. Amalgamation distance

The amalgamation distance, or life-span distance, was defined by [25] as the average distance that a structure travels in its life-span before merging into a bigger structure. [25] found a value equal to $4.3\delta_\omega$ by following the structures paths through flow visualisation images. [28] obtained this distance from hot wire anemometry data computing the decrease of the maxima of the cross correlation coefficients $R_{uu}(x, \xi_x, \tau)$ fitted with the function $\exp(\sqrt{-\tau/2T_v})$. The value of the amalgamation distance is then calculated as $\ell_v = T_v U_c$. These values are in quite good agreement with respect to the scattering lengths reported in the literature. However, [27], using the same approach on LES data, obtained values between 1.45 and 2.17, too low compared to the values obtained from the acoustic spectra or the values reported by [25] and [28]. [27] suggests that $\exp(\sqrt{-\tau/2T_v})$ does not fit with the maxima of the cross-correlation function suggesting that the method proposed by [28], applied to their data, is not capable of educing the scattering lengthscale computed from the acoustic spectra.

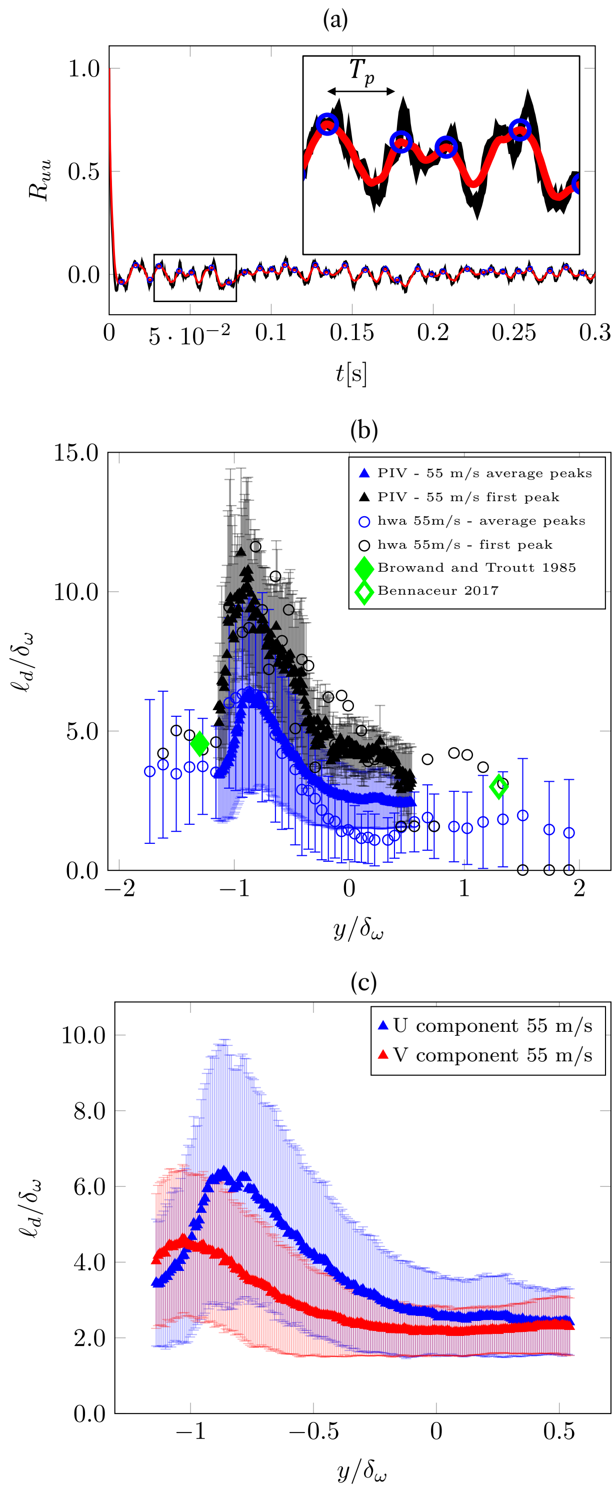

Fig. 12 (a) Autocorrelation function R_{uu} at $x = x_s$ on the low speed region, smoother in red, in blue the identification of the maxima, (b) distance calculated using the first peak [26] and the average distance between the peaks [27], comparison with hwa data (c) distance calculated using the U and V component for the method of the average peak. Errorbars indicate the standard deviation of the different RUNs.

		ℓ/δ_ω
Bennaceur et al. (2015) [29]	PSD spectrum	3.6-4.2
Kroeber et al. (2013) [4]	PSD spectrum	4.3
Sijtsma et al. (2014) [3] - DNW-LLF tunnel	PSD spectrum	4.2
Sijtsma et al. (2014) [3] - NLR-KAT tunnel	PSD spectrum	4.0
Candel et al. (1976) [23]	PSD spectrum	3.2
McAlpine et al. [30]	theoretical	4.4
Brown and Roshko (1974) [25]	average distance	3
Brown and Roshko (1974) [25]	amalgamation distance	4.3
Bennaceur et al. (2016)[12]	amalgamation distance	1.4-2.2
Bennaceur et al. (2016) [12]	average distance	3-3.2
Browand and Troutt (1985) [26]	average distance	4.54
current results	PSD spectrum (average)	4.1 ± 0.7
current results	$U\ \lambda_{\text{SPOD},U}/\delta_\omega$ (average RUNS)	5.9 ± 0.1
current results	$V\ \lambda_{\text{SPOD},V}/\delta_\omega$ (average RUNS)	4.1 ± 0.6
current results	average distance (average $\overline{T_p}$)	3.7 ± 1.8
current results	average distance (first peak T_{p1})	4.3 ± 1.8

Table 2 Lengthscales, first block literature results on aerodynamics calculations, second block lengthscale derived from acoustic measurements, third block current aerodynamic and acoustic results.

IV. Discussion and final remarks

In the haystacking community, as shown in table 2 the problem is always treated in terms of a characteristic length-scale that interacts with the acoustic wave and is responsible for the scattering. As reported above, this lengthscale has characteristic dimensions larger than four times the vorticity thickness. However, it has to be underlined that the largest scale in the shear layer is the integral lengthscale that is approximately equal to only 0.3 times the vorticity thickness [17, 31]. Conversely, the lengthscale that interacts with the acoustic transmission can be seen as a wavelength of a coherent motion associated with a certain reduced frequency; this approach helps to reveal a physical meaning behind the haystacking.

When plotted in terms of Strouhal number (using the vorticity thickness and the convection velocity), the side-lobes spectra and the SPOD spectra for the spanwise velocity component show a peak value that corresponds to a value approximately equal to 0.25 (figure 13). This Strouhal number is not dissimilar to the reduced frequency of the passage of large scale, quasi-two dimensional structures in mixing layers (0.25-0.27 according to [26]). According to [25] these structures are similar to the two dimensional roller forming due to the instability of a laminar shear layer in the pre-transition regime. This coherent motion, visible in the spanwise velocity field, and associated with a characteristic reduced frequency, consists in an alternated and oriented pattern of spanwise velocity. This is highlighted in figure 14 where the spanwise velocity field at 55 m/s is reconstructed using only the first SPOD mode and a frequency bandwidth centred at the peak frequency, filtering out all the small and less energetic turbulent scales.

Following this prospective, the haystacking and the interference between the acoustic waves and the shear layer are due to a characteristic frequency of the shear layer instantaneous spanwise velocity field rather than a large structure having a particular scale.Velocity fluctuations are "coherent" in a sense that they alternate with a "natural" frequency, generating a coherent and oriented instantaneous spanwise velocity motion. According to this scenario, instantaneously, the acoustic wave interacts mainly with the instantaneous velocity parallel to the acoustic propagation direction (acoustic wave vector). This would lead to a time delay or anticipation of the acoustic signal with respect to the baseline condition with no-flow. [3] proposed a method to calculate this time delay using the phase variation between a reference microphone in the source and the microphone placed outside the shear layer. In addition they derived an analytical formulation that links the formation of sidelobes (the haystacking) with the time delay or anticipation. The time delay/anticipation has been calculated and it is shown in figure 15 for the no-flow condition and for 35 and 55 m/s. In agreement with the scenario proposed here, the time delay/anticipation is negligible with no flow and is not negligible

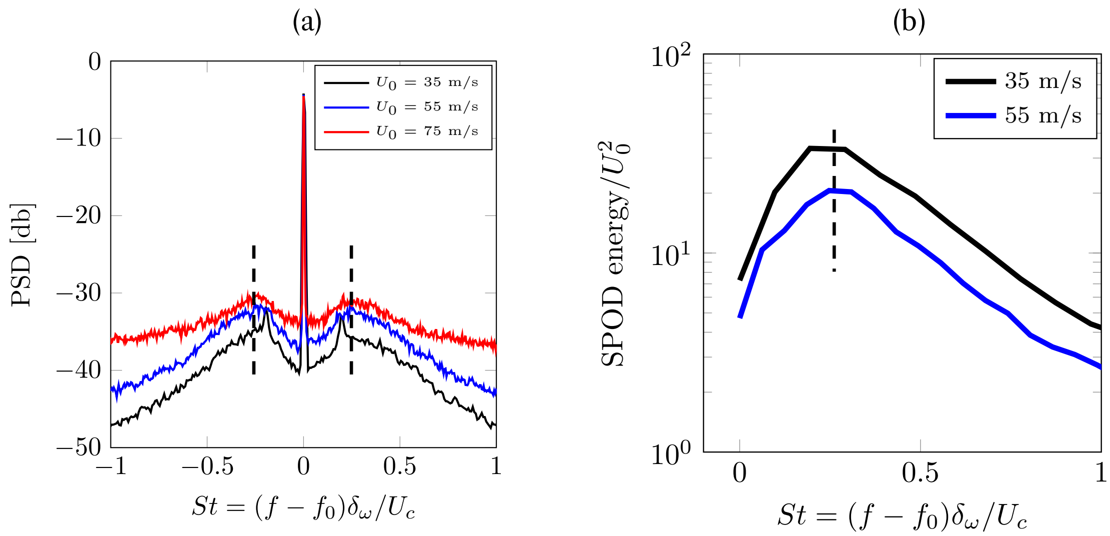

Fig. 13 (a) PSD for of the pressure signal at $x_m = x_s$, at the three free-stream velocities U_0 at f_0 =16 kHz (b) SPOD spectra of the most energetic mode for $U_0 = 35$ and 55 m/s plotted against the Strouhal number based on the vorticity thickness.

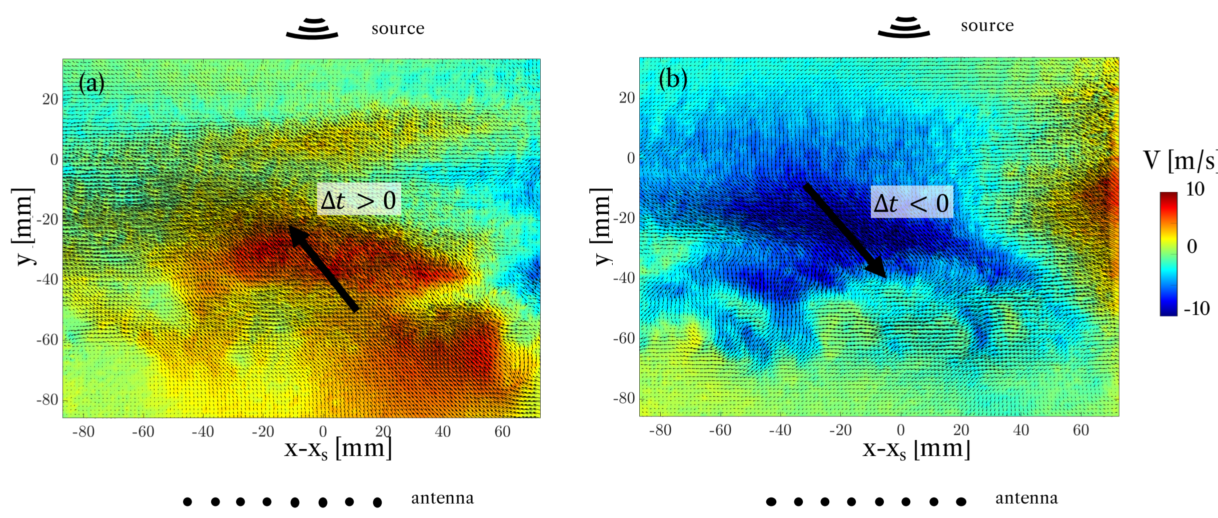

Fig. 14 Spanwise velocity field at 55 m/s reconstructed using the first SPOD mode in a frequency interval of 30-100 Hz (a) oriented positive velocity (b) oriented negative velocity.

with the flow condition, increasing when the free-stream velocity is increased. This confirms indeed that the scattering increases when increasing the free-stream velocity. In a companion paper we focus on the correlation of the time delay/anticipation and the spanwise velocity signal [32].

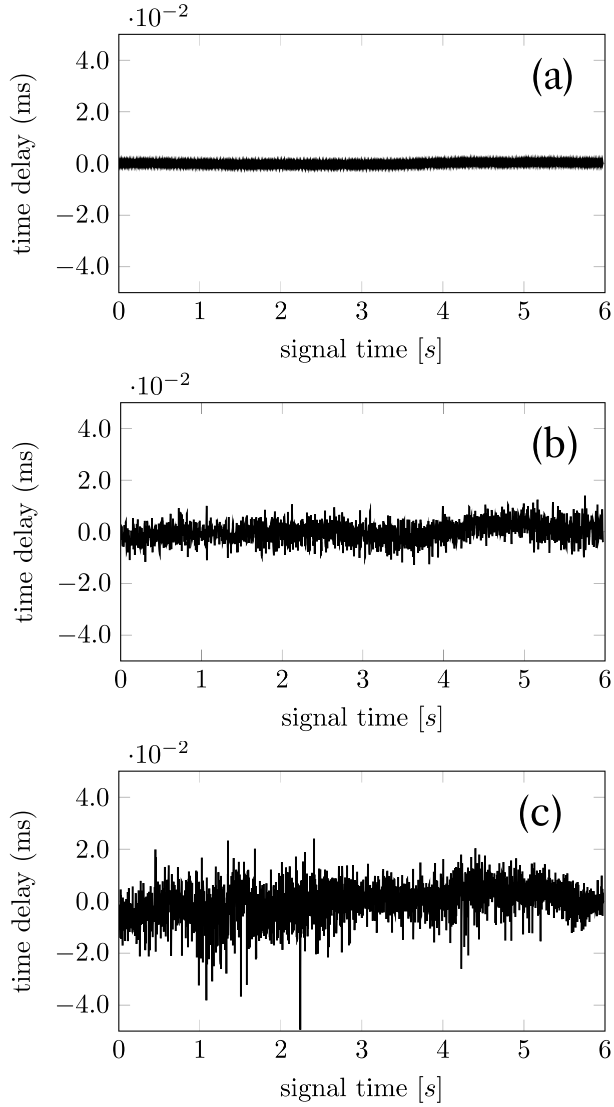

Fig. 15 Time delay between the reference microphone located in the source casing and the microphone on the antenna for (a) no flow, (b) 35 m/s **and (c)** 75 m/s **(portion of the entire signal).**

Acknowledgments

The present study is part of the program MAMBO "Méthodes avancées pour la modélisation du bruit moteur et avion" (Advanced methods for engine and aicraft noise modelling), coordinated by Airbus SAS. It was supported by the Direction Générale de l'Aviation Civile (DGAC) under the Grant n° 2021-50. This work was also performed within the framework of the Labex CeLyA of the Université de Lyon, within the programme Investissements d´Avenir (ANR-10-LABX-0060/ANR-16-IDEX-0005) operated by the French National Research Agency.

References

[1] McAlpine, A., Powles, C., and Tester, B., "A weak-scattering model for turbine-tone haystacking," *Journal of Sound and Vibration*, Vol. 332, No. 16, 2013, pp. 3806–3831. https://doi.org/10.1016/j.jsv.2013.02.023, URL https://linkinghub.elsevier.com/retrieve/pii/S0022460X13001764.

[2] Ewert, R., Kornow, O., Delfs, J., Roeber, T., and Rose, M., "A CAA Based Approach to Tone Haystacking," *15th AIAA/CEAS Aeroacoustics Conference (30th AIAA Aeroacoustics Conference)*, American Institute of Aeronautics and Astronautics, Miami, Florida, 2009. https://doi.org/10.2514/6.2009-3217, URL https://arc.aiaa.org/doi/10.2514/6.2009-3217.

[3] Sijtsma, P., Oerlemans, S., Tibbe, T. G., Berkefeld, T., and Spehr, C., "Spectral Broadening by Shear Layers of Open Jet Wind Tunnels," *20th AIAA/CEAS Aeroacoustics Conference*, American Institute of Aeronautics and Astronautics, Atlanta, GA, 2014. https://doi.org/10.2514/6.2014-3178, URL https://arc.aiaa.org/doi/10.2514/6.2014-3178.

[4] Kroeber, S., Hellmold, M., and Koop, L., "Experimental Investigation of Spectral Broadening of Sound Waves by Wind Tunnel Shear Layers," *19th AIAA/CEAS Aeroacoustics Conference*, American Institute of Aeronautics and Astronautics, Berlin, Germany, 2013. https://doi.org/10.2514/6.2013-2255, URL https://arc.aiaa.org/doi/10.2514/6.2013-2255.

[5] Lighthill, M. J., "On the energy scattered from the interaction of turbulence with sound or shock waves," *Mathematical Proceedings of the Cambridge Philosophical Society*, Vol. 49, No. 3, 1953, pp. 531–551. https://doi.org/10.1017/S0305004100028693, URL https://www.cambridge.org/core/product/identifier/S0305004100028693/type/journal_article.

[6] Kraichnan, R. H., "The Scattering of Sound in a Turbulent Medium," *The Journal of the Acoustical Society of America*, Vol. 25, No. 6, 1953, pp. 1096–1104. https://doi.org/10.1121/1.1907241, URL http://asa.scitation.org/doi/10.1121/1.1907241.

[7] Candel, S., Guedel, A., and Julienne, A., "Résultats préliminaires sur la diffusion d'une onde acoustique par écoulement turbulent," *Le Journal de Physique Colloques*, Vol. 37, No. C1, 1976, pp. C1–153–C1–160. https://doi.org/10.1051/jphyscol:1976122, URL http://www.edpsciences.org/10.1051/jphyscol:1976122.

[8] Campos, L. M. B. C., "The spectral broadening of sound by turbulent shear layers. Part 2. The spectral broadening of sound and aircraft noise," *Journal of Fluid Mechanics*, Vol. 89, No. 4, 1978, pp. 751–783. https://doi.org/10.1017/S0022112078002839, URL https://www.cambridge.org/core/product/identifier/S0022112078002839/type/journal_article.

[9] Clair, V., and Gabard, G., "Spectral broadening of acoustic waves by convected vortices," *Journal of Fluid Mechanics*, Vol. 841, 2018, pp. 50–80. https://doi.org/10.1017/jfm.2018.94, URL https://www.cambridge.org/core/product/identifier/S0022112018000940/type/journal_article.

[10] Candel, S., Julienne, A., and Guedel, A., "Refraction and scattering of sound in an open wind tunnel flow," *ICIASF'75; 6th International Congress on Instrumentation in Aerospace Simulation Facilities*, 1975, pp. 288–300.

[11] Candel, S., Julliand, M., and Julienne, A., "Shielding and scattering by a jet flow," *3rd Aeroacoustics Conference*, American Institute of Aeronautics and Astronautics, Palo Alto,CA,U.S.A., 1976. https://doi.org/10.2514/6.1976-545, URL https://arc.aiaa.org/doi/10.2514/6.1976-545.

[12] Bennaceur, I., Mincu, D. C., Mary, I., Terracol, M., Larchevêque, L., and Pierre, D., "Physical Analysis of Acoustic Scattering by a Turbulent Shear Layer using Numerical Simulation," *22nd AIAA/CEAS Aeroacoustics Conference*, American Institute of Aeronautics and Astronautics, Lyon, France, 2016. https://doi.org/10.2514/6.2016-2780, URL https://arc.aiaa.org/doi/10.2514/6.2016-2780.

[13] Campos, L. M. B. C., "The spectral broadening of sound by turbulent shear layers. Part 1. The transmission of sound through turbulent shear layers," *Journal of Fluid Mechanics*, Vol. 89, No. 4, 1978, pp. 723–749. https://doi.org/10.1017/S0022112078002827, URL https://www.cambridge.org/core/product/identifier/S0022112078002827/type/journal_article.

[14] Clair, V., and Gabard, G., "Numerical Investigation on the Spectral Broadening of Acoustic Waves by a Turbulent Layer," *22nd AIAA/CEAS Aeroacoustics Conference*, American Institute of Aeronautics and Astronautics, Lyon, France, 2016. https://doi.org/10.2514/6.2016-2701, URL https://arc.aiaa.org/doi/10.2514/6.2016-2701.

[15] Michaelis, D., Neal, D. R., and Wieneke, B., "Peak-locking reduction for particle image velocimetry," *Measurement Science and Technology*, Vol. 27, No. 10, 2016, p. 104005. https://doi.org/10.1088/0957-0233/27/10/104005, URL https://iopscience.iop.org/article/10.1088/0957-0233/27/10/104005.

[16] Perry, A., *Hot-wire anemometry*, Oxford University Press, 1982.

[17] Bell, J. H., and Mehta, R. D., "Development of a two-stream mixing layer from tripped and untripped boundary layers," *AIAA Journal*, Vol. 28, No. 12, 1990, pp. 2034–2042. https://doi.org/10.2514/3.10519, URL https://arc.aiaa.org/doi/10.2514/3.10519.

[18] Görtler, H., "Berechnung von Aufgaben der freien Turbulenz auf Grund eines neuen Näherungsansatzes ." *ZAMM - Zeitschrift für Angewandte Mathematik und Mechanik*, Vol. 22, No. 5, 1942, pp. 244–254. https://doi.org/10.1002/zamm.19420220503, URL https://onlinelibrary.wiley.com/doi/10.1002/zamm.19420220503.

[19] Bennaceur, I., Mincu, D., Mary, I., Terracol, M., Larchevêque, L., and Dupont, P., "Numerical simulation of acoustic scattering by a plane turbulent shear layer: Spectral broadening study," *Computers & Fluids*, Vol. 138, 2016, pp. 83–98. https://doi.org/10.1016/j.compfluid.2016.08.012, URL https://linkinghub.elsevier.com/retrieve/pii/S0045793016302584.

[20] Kim, Y. C., and Powers, E. J., "Digital Bispectral Analysis and Its Applications to Nonlinear Wave Interactions," *IEEE Transactions on Plasma Science*, Vol. 7, No. 2, 1979, pp. 120–131. https://doi.org/10.1109/TPS.1979.4317207, URL http://ieeexplore.ieee.org/document/4317207/.

[21] Schmidt, O. T., and Colonius, T., "Guide to Spectral Proper Orthogonal Decomposition," *AIAA Journal*, Vol. 58, No. 3, 2020, pp. 1023–1033. https://doi.org/10.2514/1.J058809, URL https://arc.aiaa.org/doi/10.2514/1.J058809.

[22] Towne, A., Schmidt, O. T., and Colonius, T., "Spectral proper orthogonal decomposition and its relationship to dynamic mode decomposition and resolvent analysis," *Journal of Fluid Mechanics*, Vol. 847, 2018, pp. 821–867. https://doi.org/10.1017/jfm.2018.283, URL https://www.cambridge.org/core/product/identifier/S0022112018002835/type/journal_article.

[23] Candel, S., Guedel, A., and Julienne, A., "Radiation, refraction and scattering of acoustic waves in a free shear flow," *3rd Aeroacoustics Conference*, American Institute of Aeronautics and Astronautics, Palo Alto,CA,U.S.A., 1976. https://doi.org/10.2514/6.1976-544, URL https://arc.aiaa.org/doi/10.2514/6.1976-544.

[24] Tatarski, V. I., *Wave propagation in a turbulent medium*, Courier Dover Publications, 2016.

[25] Brown, G. L., and Roshko, A., "On density effects and large structure in turbulent mixing layers," *Journal of Fluid Mechanics*, Vol. 64, No. 4, 1974, pp. 775–816. https://doi.org/10.1017/S002211207400190X, URL https://www.cambridge.org/core/product/identifier/S002211207400190X/type/journal_article.

[26] Browand, F. K., and Troutt, T. R., "The turbulent mixing layer: geometry of large vortices," *Journal of Fluid Mechanics*, Vol. 158, 1985, pp. 489–509. https://doi.org/10.1017/S0022112085002737, URL https://www.cambridge.org/core/product/identifier/S0022112085002737/type/journal_article.

[27] Bennaceur, I., "Etude numérique de la diffusion d'une onde acoustique par une couche de cisaillement turbulente à l'aide d'une simulation aux grandes échelles," Ph.D. thesis, 2017. URL http://www.theses.fr/2017AIXM0187, thèse de doctorat dirigée par Dupont, Pierre et Larchevêque, Lionel Sciences de l'ingénieur. Mécanique et physique des fluides Aix-Marseille 2017.

[28] Guédel, A., "Diffusion d'un champ acoustique par un écoulement inhomogène et non uniforme," Ph.D. thesis, 1985.

[29] Bennaceur, I., Mincu, D.-C., Mary, I., Terracol, M., Larcheveque, L., and Pierre, D., "Numerical simulation of spectral broadening of an acoustic wave by a spatially growing turbulent mixing layer," *21st AIAA/CEAS Aeroacoustics Conference*, American Institute of Aeronautics and Astronautics, Dallas, TX, 2015. https://doi.org/10.2514/6.2015-2841, URL https://arc.aiaa.org/doi/10.2514/6.2015-2841.

[30] McAlpine, A., Powles, C., and Tester, B., "A Weak Scattering Model for Tone Haystacking," *15th AIAA/CEAS Aeroacoustics Conference (30th AIAA Aeroacoustics Conference)*, American Institute of Aeronautics and Astronautics, Miami, Florida, 2009. https://doi.org/10.2514/6.2009-3216, URL https://arc.aiaa.org/doi/10.2514/6.2009-3216.

[31] Wygnanski, I., and Fiedler, H. E., "The two-dimensional mixing region," *Journal of Fluid Mechanics*, Vol. 41, No. 2, 1970, pp. 327–361. https://doi.org/10.1017/S0022112070000630, URL https://www.cambridge.org/core/product/identifier/S0022112070000630/type/journal_article.

[32] Chambon, J., Minck, O., Bouley, S., Scarano, F., and Pereira, A., "PIV based coherence loss correction for acoustic imaging in open jet wind tunnels," *30th AIAA/CEAS Aeroacoustics Conference*, American Institute of Aeronautics and Astronautics, Rome, Italy, 2024.